IEEE Photonics Journal
An IEEE Photonics Society Publication

# A Slot-Based Surface Plasmon-Polariton Waveguide With Long-Range Propagation and Superconfinement

Volume 4, Number 3, June 2012

G. X. Cai
M. Luo
Z. P. Cai
H. Y. Xu
Q. H. Liu, Fellow, IEEE

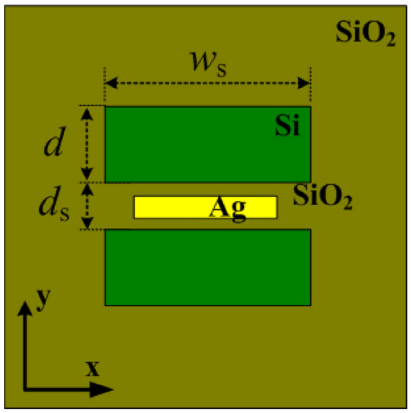


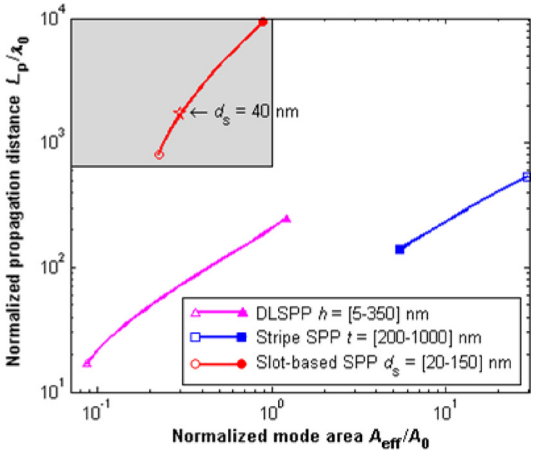


DOI: 10.1109/JPHOT.2012.2198914
1943-0655/$31.00 ©2012 IEEE

# A Slot-Based Surface Plasmon-Polariton Waveguide With Long-Range Propagation and Superconfinement

**G. X. Cai,[1,2] M. Luo,[2] Z. P. Cai,[1] H. Y. Xu,[1] and Q. H. Liu,[2] *Fellow, IEEE***

[1]Institute of Optoelectronic Technology, Department of Electronic Engineering, Xiamen University, Xiamen 361005, China
[2]Department of Electrical and Computer Engineering, Duke University, Durham, NC 27708 USA

*DOI: 10.1109/JPHOT.2012.2198914*


Manuscript received April 30, 2012; accepted May 3, 2012. Date of publication May 16, 2012; date of current version May 23, 2012. Corresponding author: Q. H. Liu (e-mail: qhliu@duke.edu).

**Abstract:** A full-vector spectral element method (SEM) is applied to model and simulate surface plasmon-polariton (SPP) waveguides. Gauss–Lobatto–Legendre (GLL) polynomials are used to construct higher-order basis functions to achieve spectral accuracy. A discretization scheme featuring a nonuniform mesh with extra elements near the metal–dielectric interface is proposed to capture the waveguide configuration and dramatical mode field variations of the SPP waveguide. The studies on the accuracy and mode field distribution show that SEM is highly efficient and accurate. Using SEM simulation, a slot-based SPP waveguide operating at telecom wavelengths is proposed. Numerical results show that the proposed structure can simultaneously achieve millimeter-scale propagation distance ($L_p \sim 2.6$ mm) and below-diffraction-limited effective mode area ($A_{eff}/A_0 \sim 0.3$). Parametric plots illustrate a significant improvement when compared to conventional SPP waveguides. Investigation of the mode width and crosstalk also demonstrates the excellent 3-D integration performance of the structure. The proposed slot-based SPP waveguide thus can become a potential candidate for highly integrated photonic circuits.

**Index Terms:** Plasmonics, subwavelength structures, waveguides.

## 1. Introduction

Miniaturized integrated photonic circuits with length scales much smaller than operation wavelength are attracting significant research interests. Subwavelength waveguides and devices have been proposed and demonstrated based on various technologies, e.g., photonic crystal waveguides [1], [2], slot waveguides [3], [4], and surface plasmon-polariton (SPP) waveguides [5]–[7]. Unlike the former two candidate waveguides, SPP waveguides can provide subwavelength confinement, even with the potential of breaking the diffraction limit. This compact confinement results from its ability of exploiting the coupling between electromagnetic fields and oscillations of the conductor's electron plasma. Moreover, due to the property of concentrating energy at the metal–dielectric interface and the existence of metal, SPP waveguides provide the possibility of easy-achieving optical nonlinearities [8], [9] and introducing thermooptic effects [10], [11] or electrooptic effects [12] by using the same metal as electrodes. The control signal propagating in an SPP waveguide is more accessible. The SPP waveguide is one of the most promising candidates for highly integrated photonic circuits.

Previously reported SPP waveguide geometry included metal slabs, metal stripes, metal nanoparticle waveguides, dielectric-loaded SPP (DLSPP) waveguides, etc. [7]. However, due to the intrinsic loss of metal, propagation distance of light in SPP waveguides is usually small under

compact confinement. Thus the tradeoff between propagation distance and confinement becomes critical in an SPP waveguide. Recently, significant efforts have been dedicated to increasing the propagation distance without loosening the confinement. Two design principles are employed. One is to achieve a symmetric SPP mode [13], [14], whose dominant transverse component of electric field has even symmetry, while its longitudinal component has odd symmetry with respect to the midplane of the metal. As the longitudinal component of electric field in the metal determines the SPP damping, when it crosses zero at the midplane of the metal, the corresponding mode will experience small attenuation and propagate a long distance. It is conventionally called the long-range SPP (LR-SPP) mode [7], [15]. The other principle takes advantage of a hybrid configuration consisting of high-permittivity and low-permittivity dielectric materials simultaneously. The SPP mode that approaches the light line of the low-permittivity dielectric has a small propagation constant, thus the propagation distance determined by the imaginary part of propagation constant will be large [16], [17]. Electromagnetic energy will be stored and transmitted in low-permittivity region which is confined by the high-permittivity materials [18], [19]. These two principles can be also combined to increase the propagation distance [20]–[24]. With these approaches, SPP waveguides can be designed to have mm-scale propagation. However, the mode confinement is still equal to or larger than the diffraction limit. It is thus desirable to design an SPP waveguide characterized simultaneously by mm-scale propagation distance and below-diffraction-limited effective mode area.

Designing an SPP waveguide requires the analysis of modes of a vector wave equation in 2-D cross section. Numerical techniques involving a discretization scheme must be applied to determine the modes when the geometry is complex. In the past, several numerical methods have been developed to analyze the SPP propagation characteristics, including the method of lines (MoL), the finite element method (FEM), the finite difference method (FDM), the finite difference time domain (FDTD) method, etc. [25], [26]. However, these conventional methods still face great challenges since SPP waveguides possess peculiar configuration and field distributions, especially the intensive mode field concentration and variation in nanoscale regions near the metal. For the most common FEM, it would require extremely fine sampling points to capture the dramatic mode field variation within a narrow region, thus leading to great computational consumption. In order to overcome these difficulties, high-order methods such as the multidomain pseudospectral scheme [26] have been developed [27]. Here, we applied the spectral element method (SEM) for the first time to simulate SPP waveguides.

The SEM is a special type of higher-order FEM, with different choice of basis functions and quadrature integration. The high-order basis functions are constructed by Gauss–Lobatto–Legendre (GLL) polynomials, thus providing the ability to precisely simulate the spatially abrupt changes of permittivity within a narrow region. SEM has been applied to the determination of band structures of photonic crystals and proved to have spectral accuracy with the error decreasing exponentially with the order of basis functions [28], [29].

In this present paper, two typical SPP waveguides were investigated firstly to demonstrate the advantages of SEM, including detailed analysis of convergence, accuracy and mode field distribution. Then a slot-based SPP waveguide with long-range propagation and superconfinement was designed and its performance was studied. This SPP waveguide is a promising candidate for 3-D integrated photonic circuits.

## 2. Method and Validation

The SEM solves the electric field vector Helmholtz equation and obtains the propagation constant $\beta$. By assuming fields in a time-harmonic form $\mathbf{E}(x, y, z)\exp(j\omega t)$, the full-vector Helmholtz equation of electric field is described as

$$\nabla \times \left[\mu_r^{-1}(\nabla \times \mathbf{E})\right] - k_0^2 \varepsilon_r \mathbf{E} = 0 \tag{1}$$

where $k_0 = \omega/c$ is the wavenumber in vacuum, $\mu_r$ and $\epsilon_r$ are relative permeability and relative permittivity tensors. In general, the media in an SPP waveguide are considered as isotropic, leading

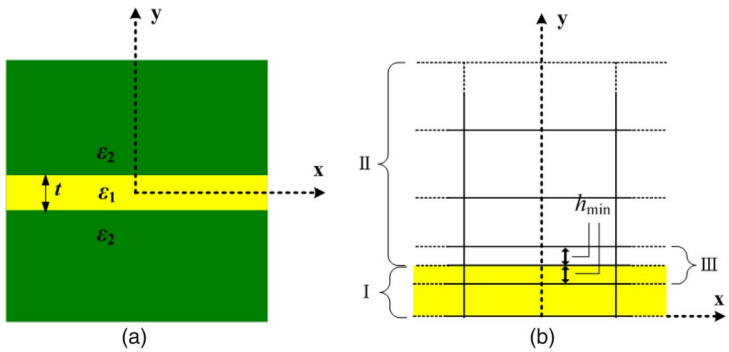


Fig. 1. Metal slab SPP waveguide for validation of SEM. (a) Cross section of the waveguide. (b) SEM discretization scheme for the upper-half portion of the metal slab.

$\mu_r$ and $\epsilon_r$ to be scalar values. With SPP propagating along the $+z$ direction, in which the guiding structure is invariant, the electric field can be expressed as

$$\mathbf{E}(x, y, z) = \mathbf{e}(x, y)\exp(-j\beta z) \tag{2}$$

where **e** is a 2-D vector field that only depends on the transverse coordinates $(x, y)$, $\beta = \beta' - j\beta''$ is the complex propagation constant of the mode. One has $\nabla = \nabla_t - j\beta\hat{z}$. $\beta'$ is the phase constant and $\beta''$ is the attenuation constant. The mode effective index is then given by $N_{\text{eff}} = \beta'/k_0$, and the propagation distance of the SPP mode is $L_p = 1/(2\beta'')$.

In the SEM, the electric field in the computational domain is expanded by the spectral element basis functions $\Phi_i$ as follows:

$$\mathbf{e} = \sum_i e_i \Phi_i. \tag{3}$$

Substituting (2) and (3) into (1), and applying the Galerkin method with SEM's basis function, the weak form of the full-vector Helmholtz equation for electric field is given as

$$\int \left[\nabla \times \Phi_i \cdot \mu_r^{-1} \cdot \nabla \times \mathbf{e} - j\beta\left(\nabla \times \Phi_i \cdot \mu_r^{-1} \cdot \hat{z} \times \mathbf{e} - \hat{z} \times \Phi_i \cdot \mu_r^{-1} \cdot \nabla_t \times \mathbf{e}\right) + \beta^2(\hat{z} \times \Phi_i \cdot \hat{z} \times \mathbf{e}) - k_0^2 \Phi_i \cdot \varepsilon_r \cdot \mathbf{e}\right] dS = 0. \tag{4}$$

The SEM is then applied to solve (4) [28]–[32]. The GLL polynomials are used to construct basis functions in a quadrilateral mesh. For 2-D problems, a basis function is written as the tensor product of two 1-D basis functions in the reference square element. The positions of nodal points thus form an interesting distribution which is denser near the edge of an discretized element than in the middle of it [28], [29]. Because the SPP field would dramatically change near the metal–dielectric interface, this SEM nodal point distribution is suitable for simulating the SPP waveguides.

To apply SEM, a reasonable discretization scheme is also essential. Following the feature of SPP mode distribution, a nonuniform mesh is utilized with extra elements near the metal–dielectric interface. This discretization scheme assigns more nodal points to the region where mode field changes rapidly to model it accurately, and fewer points to the region where mode field changes smoothly to save computational resources. The following two numerical examples of metal slab and metal stripe will show the construction of this mesh and the validation of SEM.

### 2.1. Validation for a Metal Slab

The metal slab SPP waveguide case shown in Fig. 1(a) comes from [25]. It has the symmetric insulator–metal–insulator (IMI) configuration featuring a thin metal film of relative permittivity $\epsilon_1$ and thickness $t$ being embedded in a dielectric background of relative permittivity $\epsilon_2$, which extends

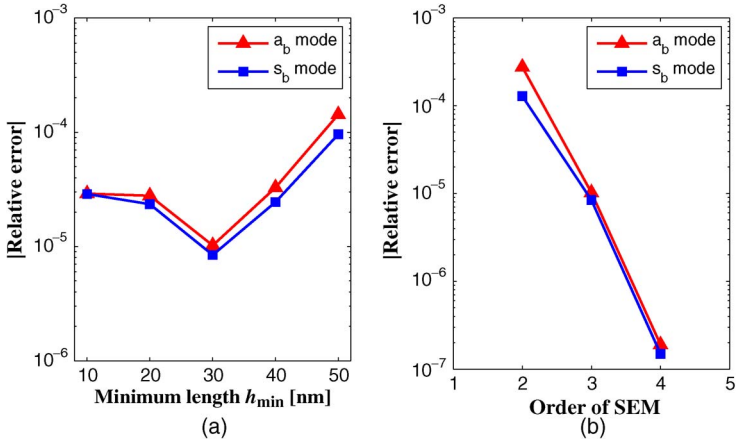


Fig. 2. Error for the metal slab in Fig. 1(a). (a) Absolute relative error of propagation constant versus the minimum element length. (b) Absolute relative error of propagation constant versus the order of SEM basis functions when an optimum $h_{min}$ is chosen. Convergences of both $a_b$ mode and $s_b$ mode are listed. Reference data are analytical solution.

infinitely on both sides of the film. Two purely bound TM modes, denoted as $a_b$ and $s_b$, having asymmetric and symmetric spatial distributions with respect to $x$ axis for $E_y$ component, respectively, are supported by this waveguide [15], [16]. $\epsilon_1 = -19 - 0.53j$ and $\epsilon_2 = 4$ at the operation wavelength $\lambda_0 = 633$ nm, and $t = 100$ nm. In fact, this slab geometry can be solved using a 1-D method. However, we do it using 2-D SEM, to verify its accuracy.

Fig. 1(b) gives the upper-half portion of the whole SEM discretization scheme for the metal slab. For the horizontal direction ($x$ axis), it can be evenly divided, since there is no dielectric variation over this direction. Here, 3 elements are divided for the convenience to implement the algorithm. For the vertical direction ($y$ axis), it can be divided into two regions according to the waveguide configuration, Region I for metal and Region II for dielectric. Region II is further discretized using an equidistance line spacing. Typically the distance is chosen as $\lambda_0/3$. Then extra elements are added near materials interfaces to capture the change of electromagnetic fields. Since fields would vary rapidly in a metal–dielectric interface, the line spacing $h_{min}$ of Region III is set to be the minimum length of all elements. Small $h_{min}$ is used to achieved reasonable accuracy. For conventional methods, it will require large computational efforts [25]. For SEM, the number of unknowns will not be changed by $h_{min}$, providing the possibility to adjust it without additional computational efforts. Periodic boundary condition is applied for this simulation and computation domain should be as large as possible to minimize the coupling from adjacent periods. Since this metal slab SPP waveguide configuration has loose confinement, the side length of computation domain is set to be $\sim 3\lambda_0$.

Fig. 2(a) and (b) show the error of SEM simulation, which used $3 \times 14$ elements. Reference data are analytical solutions [33]. Fig. 2(a) gives the absolute relative error of propagation constant of $a_b$ and $s_b$ modes as a function of $h_{min}$. SEM order is chosen as 3, and the number of unknowns is 1237 for all $h_{min}$. It can be seen that there exists an optimum $h_{min} = 30$ nm and the absolute relative error is better than $10^{-5}$. The errors get worse while $h_{min}$ decreases. This is because the mismatch between elements in Region III and its adjacent regions will introduce errors when a small $h_{min}$ is used.

The convergence with respect to the order of SEM was then shown in Fig. 2(b). The results indicate that convergence to an absolute relative error of $< 0.1\%$ can be easily achieved, and the absolute relative error decreases exponentially as the order increases, proving the spectral accuracy property for the SEM. This rapid convergence speed is also valid for other $h_{min}$.

The field profiles of the SPP modes are supposed to be difficult to accurately capture, especially for the region near the metal–dielectric interface [27], [34]. With the help of extra elements, SEM possesses the ability to simulate the abrupt changes of permittivity within a narrow region. Fig. 3 shows the comparison of $s_b$ mode field distributions between the analytical solutions [33] and the

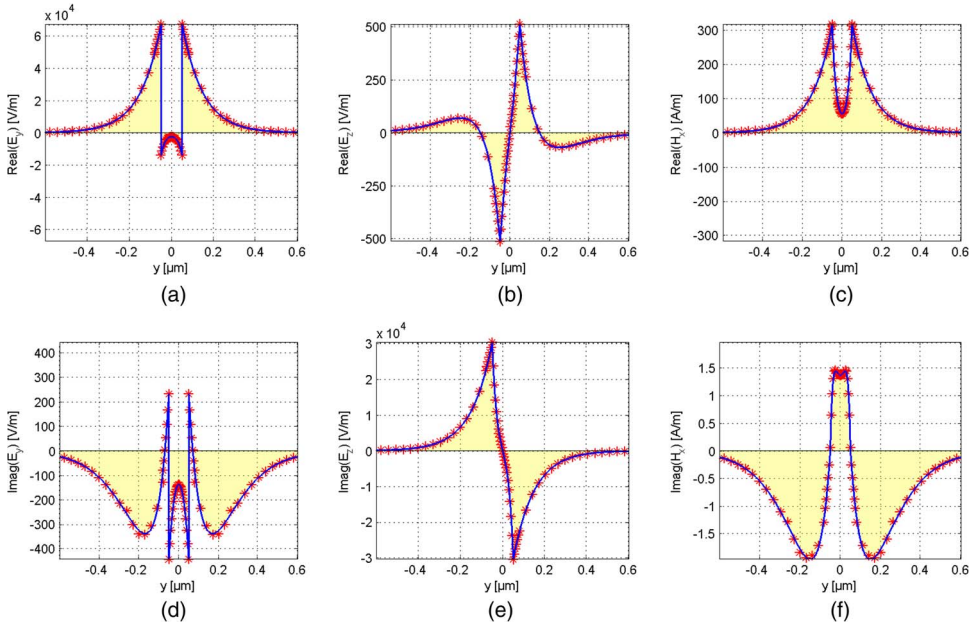


Fig. 3. Comparison of $s_b$ mode field distributions, (a)–(c) are real part of $E_y$, $E_z$ and $H_x$, respectively, and (d)–(f) imaginary part of them. Lines are results from analytical solutions, and star symbols are SEM results.

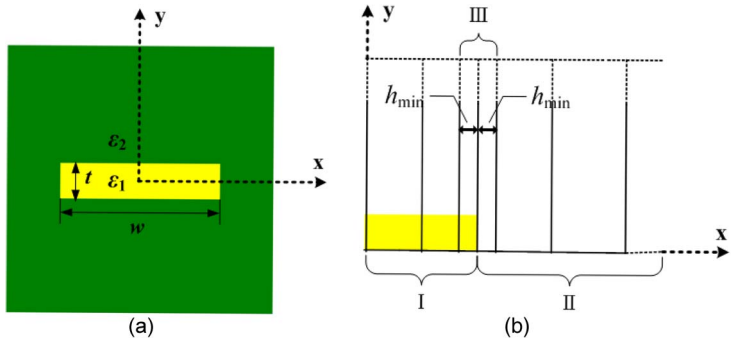


Fig. 4. Metal stripe SPP waveguide for validation of SEM. (a) Cross section of the waveguide. (b) SEM discretization scheme for the metal stripe in the first quadrant.

numerical SEM results. Power carried by the mode has been normalized to 1 W/m width of the guide. The modes of metal slab have 3 non-zero components, which are $E_y$, $E_z$ and $H_x$. Fig. 3(a)–(c) are real part of component $E_y$, $E_z$, and $H_x$, respectively. Fig. 3(d)–(f) are the corresponding imaginary part. The comparison of $a_b$ mode is not shown here for simplicity. It can be seen that SEM has successfully retrieved the field profiles of $s_b$ mode and it fits well to the analytical results.

### 2.2. Validation for a Metal Stripe

The metal stripe SPP waveguide has analogous configuration to the above slab case, except for a finite width $w$. Here, we choose $w = 1$ $\mu$m to conveniently compare with published reference [25]. Fig. 4(a) shows the geometry of this metal stripe. Bound modes supported by this waveguide are either asymmetric or symmetric with respect to $x$ axis and $y$ axis for their $E_y$ component [15], [16]. Fig. 4(b) gives the SEM discretization scheme for only a quarter portion of the metal stripe in

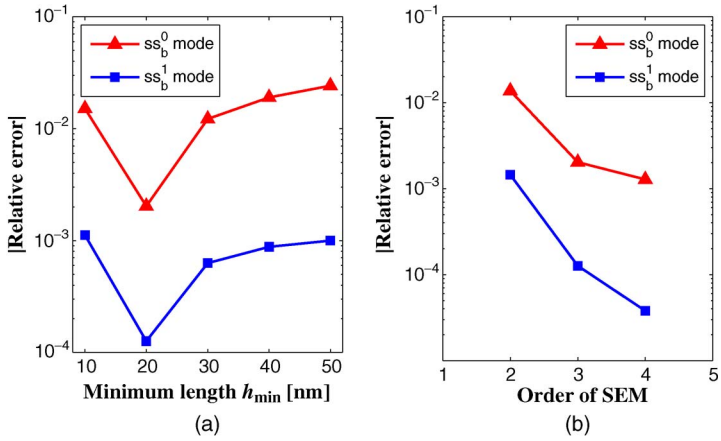


Fig. 5. Error for the metal stripe in Fig. 4(a). (a) Absolute relative error of propagation constant versus the minimum element length. (b) Absolute relative error of propagation constant versus the order of SEM basis functions when an optimum $h_{min}$ is chosen. Convergences are shown for both $ss_b^0$ mode and $ss_b^1$ mode. Reference data are MoL results from [25].

Fig. 4(a). The discretization mesh in the vertical direction ($y$ axis) is not shown for its resemblance to the metal slab case. The discretization of the horizontal direction ($x$ axis) is similar to that of vertical direction. Region I and Region II occupy the metal and dielectric domain, respectively. Both are discretized using an equidistance line spacing. Typically the distance is chosen as $\lambda_0/3$. Region III adds extra elements near the metal–dielectric interface, which has a line spacing $h_{min}$. For modeling open structures (e.g., metal stripe waveguide), absorbing boundary conditions are placed at outer perimeter of the computation domain.

Fig. 5 gives the convergence investigation of the SEM simulation. It used 192 elements, with 12 along the horizontal direction and 16 along the vertical direction, respectively. Reference data are MoL results from [25]. The study on the absolute relative error of propagation constant of $ss_b^0$ and $ss_b^1$ modes (one from fundamental modes and one from higher-order modes, respectively) as a function of $h_{min}$ was shown in Fig. 5(a). SEM order is chosen as 3. It can be seen that the lowest absolute relative error was achieved synchronously at $h_{min} = 20$ nm. Then the convergence at this optimum $h_{min}$ with respect to the order of SEM was shown in Fig. 5(b). Conclusions can be drawn from these results. First, an acceptable absolute relative error of 1% was easily achieved when the order of SEM is 3, and the error converged exponentially as the order increased. Secondly, convergence was exponentially fast for both fundamental and higher-order modes at a same speed. This is derived from the reasonable discretization scheme shown in Fig. 4(b), which covers uniformly for both subwavelength-varied mode field area and macroscale region of the waveguide. However, $ss_b^0$ mode had a worse absolute relative error than $ss_b^1$ mode, since its localization is much stronger than the later one.

The computational effort of SEM is much less than that of FEM. For metal stripe case to achieve an error of 1%, SEM used 6997 unknowns (192 elements, order 3). It took 34 seconds of CPU time and 120 MB of memory in a regular laptop, proving the great efficiency and accuracy of SEM. In contrast, the FEM requires much more unknowns ($\sim$79000) to achieve the same error, which takes 77 seconds of CPU time and 310 MB of memory using commercial software package COMSOL™. From the analysis of two typical numerical examples, SEM was proved to be a highly efficient and accurate method for SPP waveguides. It can be reliably applied to design new SPP waveguides for integrated photonic circuits application.

## 3. Slot-Based SPP Waveguide Configuration and Modal Properties

Applying SEM simulation at telecommunication wavelength, $\lambda_0 = 1550$ nm, the proposed slot-based SPP waveguide is designed as follows. As shown in Fig. 6(a), two silicon bulks (refractive

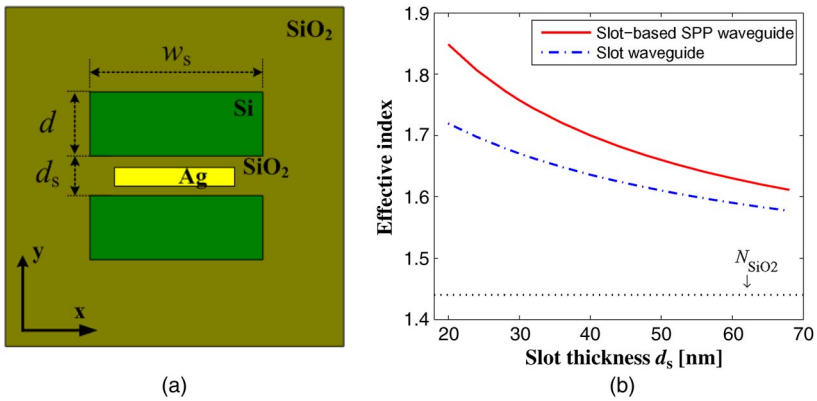


Fig. 6. Proposed slot-based SPP waveguide. (a) Cross section. (b) The effective index versus the slot thickness $d_s$ for this SPP waveguide and a slot waveguide of the same dimensions.

index $n_{Si} = 3.48$) of width $w_s = 300$ nm and thickness $d = 140$ nm approach each other in the low-permittivity background. The low-permittivity region between them is denoted as the slot waveguide, of width $w_s$ and thickness $d_s$. $SiO_2$ material $(n_{SiO_2} = 1.44)$ is chosen to form a high-index-contrast with respect to silicon. A metal stripe is inserted into the center of slot to form the proposed slot-based SPP waveguide. We choose silver for this stripe because of its small loss tangent at the interested wavelength $(\epsilon_{Ag} = -129 - 3.3j)$ [34]. The dimensions of silver stripe are 200 nm in width and only 10 nm in thickness, for a smaller bulk of metal will bring less loss into propagation.

Generally, the long-range mode of this silver stripe waveguide surrounding by pure $SiO_2$ would be cutoff due to its small width and thickness [15]. The use of the two silicon bulks and their proximity help to produce a new long-range mode, which can be explained by the coupled mode theory. Fig. 6(b) analyzes the dependence of the effective index of the slot-based SPP waveguide $(N_{spp})$ and slot waveguide $(N_{slot})$, versus the slot thickness $d_s$. The dotted line is the refractive index of $SiO_2$ $(N_{SiO_2})$. Bound modes of a waveguide in the background material of $SiO_2$ have larger effective index than $N_{SiO_2}$, while cutoff modes have smaller index than $N_{SiO_2}$. The cutoff long-range mode of silver stripe waveguide is located beneath the dotted line, which is not shown in Fig. 6(b) for simplicity. It can be seen that as $d_s$ increases, $N_{spp}$ approaches $N_{slot}$ and the cutoff silver stripe waveguide mode, but is always larger than them. This indicates that the long-range mode of the slot-based SPP waveguide is the symmetric parity of the coupled system between slot waveguide and silver stripe waveguide. The effective index of antisymmetric parity will be smaller than that of the silver stripe, which is also below cutoff. Meanwhile, as $d_s$ increases further, $N_{spp}$ comes closer to $N_{slot}$, suggesting that the coupled effect gets weaker, and the mode of slot-based SPP waveguide will be more like that of a slot waveguide.

Fig. 7 gives the normalized profile of the dominant transverse component $E_y$ along the $y$ direction for the slot thickness $d_s = 40$ nm. Its symmetry confirms that the proposed waveguide mode is the LR-SPP. This case has the effective index $N_{spp} = 1.7$ and the propagation distance $L_p = 2.6$ mm. The mm-scale propagation is attributed to not only the symmetric mode distribution, but also to the hybrid configuration. It enables the propagation constant of the SPP mode to approach the light line of the low-permittivity $(SiO_2)$ materials, resulting a small effective index and hence large $L_p$. However, a small effective index generally means the mode field is weakly confined to the metal. In the proposed slot-based SPP waveguide, high-index silicon bulks are used to maintain compact confinement. This can be seen from the inset of Fig. 7, which presents the electric field distribution $|\mathbf{E}|$. The mode field is well confined and enhanced at the narrow region of slot due to the coupling between silicon bulk and silver stripe. This indicates a potential application to introduce optical nonlinearities and apply electric signal to modulate optical signals.

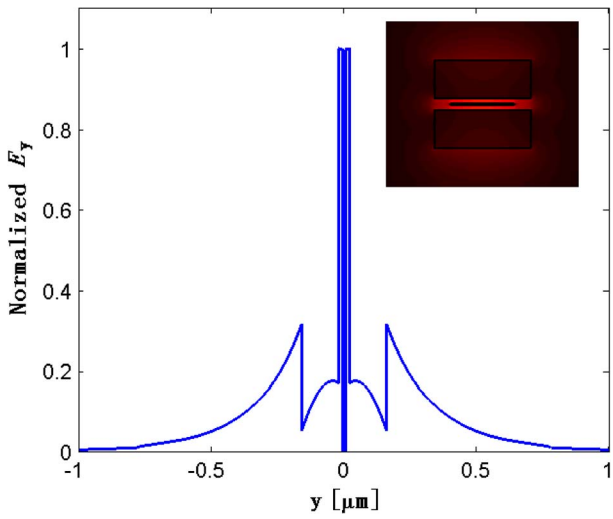


Fig. 7. Normalized profile of the dominant transverse component $E_y$ along $y$ direction for the case with the slot thickness $d_s = 40$ nm. Inset shows the electric field distribution $|\mathbf{E}|$ of the same case.

The confinement can be gauged by the normalized mode area, which is defined as $A_{\text{eff}}/A_0$, where $A_0 = (\lambda_0/2)^2$ is the diffraction-limited area in vacuum and $A_{\text{eff}}$ the statistical measure of effective mode area [35]

$$A_{eff} = \frac{\left[\int_{A\infty} W(x,y)\, dA\right]^2}{\int_{A\infty} W^2(x,y)\, dA} \tag{5}$$

where $W(x,y)$ is the mode energy density, which is calculated by the following formula:

$$W(x,y) = \frac{1}{2}\text{Re}\left\{\frac{d[\omega\varepsilon(x,y)]}{d\omega}\right\}|\mathbf{E}(x,y)|^2 + \frac{1}{2}\mu_0|\mathbf{H}(x,y)|^2. \tag{6}$$

Equation (5) is a reasonable measurement for the effective mode area since its insensitivity to strong concentration of mode field in small distances, which is typical for SPP waveguides.

To illustrate the modal properties of the proposed SPP waveguide better, we use a parametric plot, which displays the propagation distance and confinement together [18], [35]. Fig. 8 shows the parametric plot of the normalized propagation distance $L_p/\lambda_0$ versus normalized mode area $A_{\text{eff}}/A_0$. The proposed slot-based SPP waveguide is well located in the region (gray area) which has the mm-scale propagation distance and below-diffraction-limited effective mode area. The star sign labels the case of $d_s = 40$ nm, which has $L_p/\lambda_0$ of $1.7 \times 10^3$ ($L_p = 2.6$ mm) and $A_{\text{eff}}/A_0$ of 0.3. Fig. 8 also gives the parametric plots of stripe SPP waveguide (stripe SPP) and DLSPP waveguide for comparison. The stripe SPP is a silver stripe embedded in the background of $SiO_2$ material. Its dimensions are 1 $\mu$m in width and 200–1000 nm in thickness $t$, to ensure the existence of long-range mode. The DLSPP consists of a silicon bulk ($200 \times 200$ nm$^2$) and the interface of silver and $SiO_2$. The silicon bulk is embedded in $SiO_2$ region and forms a low-permittivity dielectric gap of thickness $h$ ranging from 5 to 350 nm [18]. The comparison in Fig. 8 clearly suggests that the long-range modes of the proposed slot-based SPP waveguide are significantly improved both in propagation distance and confinement when compared to those of stripe SPP waveguide. When compared to DLSPP, the proposed waveguide is one order longer in propagation distance without losing its confinement. The parametric plot clearly shows the excellent modal properties of slot-based SPP waveguide for achieving superconfinement and long-range propagation distance simultaneously, suggesting its great potential for high-density photonic circuits.

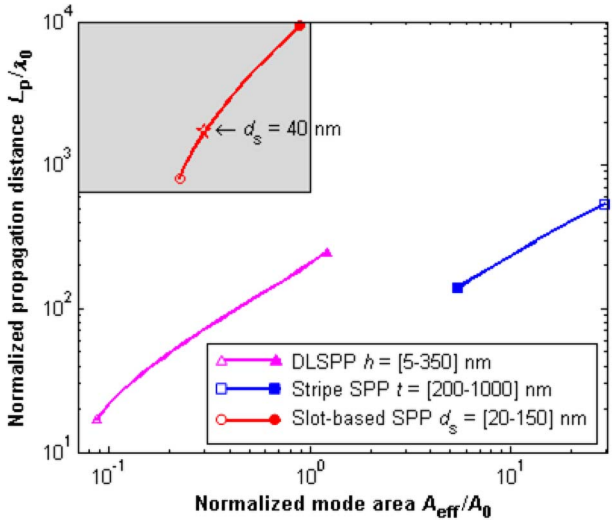


Fig. 8. Parametric plot of normalized propagation distance versus normalized mode area for the proposed slot-based SPP waveguide. The properties of stripe SPP waveguide and DLSPP waveguide are also listed for comparison.

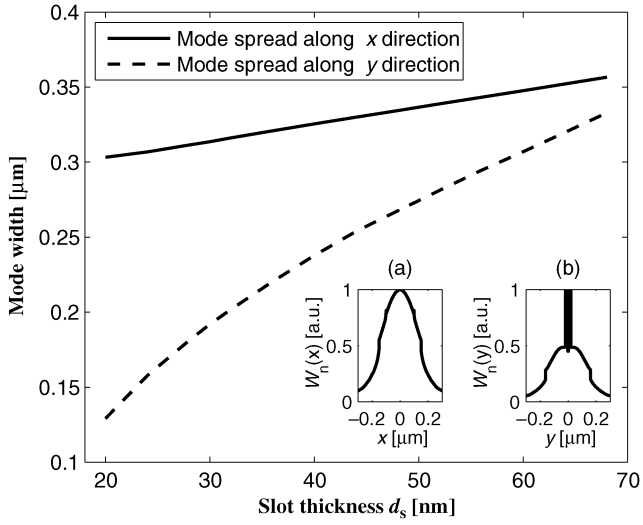


Fig. 9. Mode width along $x$ and $y$ directions versus slot thickness. The inset (a) shows the profile of normalized energy density spreading along $x$ direction for the case with the slot thickness $d_s = 40$ nm, and the inset (b) along $y$ direction.

## 4. Performance for 3-D integration

Future photonic circuits require high integration density, which is restricted by bend loss and crosstalk. The mode width, which affects the bend loss of integrated photonic circuits, is investigated firstly. Here, we considered both the horizontal $(x)$ and the vertical $(y)$ directions for mode width determination. By integrating $W(x, y)$ from (6) over $x$ and $y$ directions in the entire computation domain respectively, one can obtain the energy density profile spreading along $x$ and $y$ directions. The mode width is then defined as the full width where the energy density decays to $1/e$ of its peak value. As demonstrated in Fig. 9, both mode widths monotonically increase when slot thickness $d_s$ increases, which corresponds to the phenomenon of the increasing effective mode area with regard to increasing $d_s$. The vertical energy density has a more compact profile, due to the

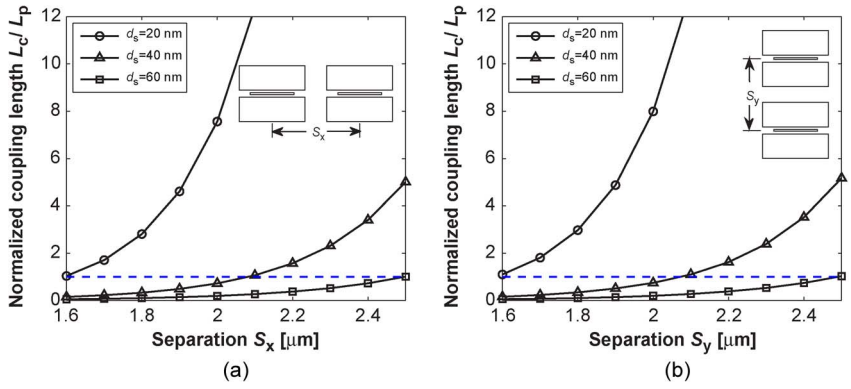


Fig. 10. Normalized coupling length of (a) horizontally parallel configuration and (b) vertically parallel configuration versus the center-to-center separation $S_x$ and $S_y$, respectively.

confinement of the high-permittivity silicon bulks. The insets of Fig. 9 also give the energy density profiles along the $x$ and $y$ directions for the case with $d_s = 40$ nm, respectively. They have been normalized by their maximum value. The mode widths for this case are 0.33 $\mu$m and 0.24 $\mu$m in $x$ and $y$ directions, respectively, suggesting significantly less bend losses than other SPP waveguides [21], [23].

Crosstalk between adjacent waveguides places a limit to the integration density of photonic circuits. It is related to the parameter of normalized coupling length $L_c/L_p$, where $L_c$ is the coupling length between two identical adjacent waveguides and $L_p$ the propagation distance of the single waveguide [21]. To ensure small crosstalk, $L_c$ should be large enough to make $L_c/L_p > 1$, which means the transmitted mode energy decays to zero before it is coupled to the adjacent waveguide core. Low crosstalk happens at large $L_c/L_p$. Using the coupled mode theory, the coupling length is calculated by $L_c = \lambda_0/2|N_s - N_a|$, where $\lambda_0$ is the operation wavelength, $N_s$ and $N_a$ are the effective indexes of the symmetric and antisymmetric modes of two adjacent waveguides, respectively. To evaluate the performance for 3-D integration, we consider two different configurations: two horizontally parallel waveguides and two vertically parallel waveguides. Fig. 10 investigates the dependence of normalized coupling length $L_c/L_p$ on the center-to-center separations $S_x$ and $S_y$, respectively. The dashed line indicates the critical normalize coupling length ($L_c/L_p = 1$). It can be seen that only small $S_x$ and $S_y$ are needed for enough isolation, e.g., 2.1 $\mu$m for both configuration of the $d_s = 40$ nm case. The crosstalk thus is significantly lower than the traditional SPP waveguides, which typically have 10 $\mu$m for the center-to-center separations [21], [23]. Combined with the mode width, the proposed slot-based SPP waveguide provides a beneficial advantage for dense 3-D integration.

## 5. Conclusion

In summary, we have applied the SEM to simulate SPP waveguides, and designed a new SPP waveguide. Owing to the nodal point distribution of GLL basis functions and the nonuniform mesh with extra elements near the metal–dielectric interface, SEM can efficiently and accurately model the SPP waveguides. The convergences of the metal slab and metal stripe SPP waveguides were analyzed. Numerical results exhibit good agreement to analytical solutions and MoL results. With an exponentially convergent behavior, SEM results can easily achieve high accuracy with absolute relative error smaller than 0.1%.

A slot-based SPP waveguide was designed and simulated by SEM. The configuration that inserts a metal strip into the core of the low-permittivity region of a slot waveguide, features a mm-scale propagation distance ($\sim$2.6 mm) and below-diffraction-limited effective mode area ($\sim 0.3A_0$, $A_0$ the diffraction-limited area in vacuum) simultaneously. Comparison shows a significant improvement against conventional SPP waveguides. The performance for 3-D integration was investigated. The

mode widths in which the energy density profile spread along *x* and *y* directions, are considerably narrow to ensure a low bend loss. The center-to-center separations were as low as 2.1 $\mu$m for both horizontally parallel and vertically parallel configurations of adjacent waveguides to ensure small crosstalk and high isolation. Together with the easy fabrication using standard lithography technique, the proposed waveguide can find its application in high-density photonic circuits.

## Acknowledgment

G. X. Cai's visit to Duke University was supported by the China Scholarship Council (CSC).

## References

[1] L. Thylén, M. Qiu, and S. Anand, "Photonic crystals—A step towards integrated circuits for photonics," *Chem. Phys. Chem.*, vol. 5, no. 9, pp. 1268–1283, Sep. 2004.
[2] G. S. Wiederhecker, C. M. B. Cordeiro, F. Couny, F. Benabid, S. A. Maier, J. C. Knight, C. H. B. Cruz, and H. L. Fragnito, "Field enhancement within an optical fibre with a subwavelength air core," *Nat. Photon.*, vol. 1, no. 2, pp. 115–118, Feb. 2007.
[3] V. R. Almeida, Q. Xu, C. A. Barrios, and M. Lipson, "Guiding and confining light in void nanostructure," *Opt. Lett.*, vol. 29, no. 11, pp. 1209–1211, Jun. 2004.
[4] Q. Xu, V. R. Almeida, R. R. Panepucci, and M. Lipson, "Experimental demonstration of guiding and confining light in nanometer-size low-refractive-index material," *Opt. Lett.*, vol. 29, no. 14, pp. 1626–1628, Jul. 2004.
[5] W. L. Barnes, A. Dereux, and T. W. Ebbesen, "Surface plasmon subwavelength optics," *Nature*, vol. 424, no. 6950, pp. 824–830, Aug. 2003.
[6] D. K. Gramotnev and S. I. Bozhevolnyi, "Plasmonics beyond the diffraction limit," *Nat. Photon.*, vol. 4, no. 2, pp. 83–91, Feb. 2010.
[7] S. I. Bozhevolnyi, *Plasmonic Nanoguides and Circuits*. Singapore: Pan Stanford Publ., 2008.
[8] G. I. Stegeman, J. J. Burke, and D. G. Hall, "Nonlinear optics of long range surface plasmons," *Appl. Phys. Lett.*, vol. 41, no. 10, pp. 906–908, Nov. 1982.
[9] A. Degiron and D. R. Smith, "Nonlinear long-range plasmonic waveguides," *Phys. Rev. A*, vol. 82, no. 3, p. 033812, Sep. 2010.
[10] G. Gagnon, N. Lahoud, G. A. Mattiussi, and P. Berini, "Thermally activated variable attenuation of long-range surface plasmon-polariton waves," *J. Lightw. Technol.*, vol. 24, no. 11, pp. 4391–4402, Nov. 2006.
[11] J. Gosciniak, S. I. Bozhevolnyi, T. B. Andersen, V. S. Volkov, J. Kjelstrup-Hansen, L. Markey, and A. Dereux, "Thermo-optic control of dielectric-loaded plasmonic waveguide components," *Opt. Exp.*, vol. 18, no. 2, pp. 1207–1216, Jan. 2010.
[12] P. Berini, R. Charbonneau, S. Jetté-Charbonneau, N. Lahoud, and G. Mattiussi, "Long-range surface plasmon-polariton waveguides and devices in lithium niobate," *J. Appl. Phys.*, vol. 101, no. 11, pp. 113114-1–113114-12, Jun. 2007.
[13] R. Adato and J. Guo, "Modification of dispersion, localization, and attenuation of thin metal stripe symmetric surface plasmon-polariton modes by thin dielectric layers," *J. Appl. Phys.*, vol. 105, no. 3, pp. 034306-1–034306-11, Feb. 2009.
[14] Y. Binfeng, H. Guohua, and C. Yiping, "Bound modes analysis of symmetric dielectric loaded surface plasmon-polariton waveguides," *Opt. Exp.*, vol. 17, no. 5, pp. 3610–3618, Mar. 2009.
[15] P. Berini, "Plasmon-polariton waves guided by thin lossy metal films of finite width: Bound modes of symmetric structures," *Phys. Rev. B, Condens. Matter Mater. Phys.*, vol. 61, no. 15, pp. 10 484–10 503, Apr. 2000.
[16] P. Berini, "Plasmon-polariton waves guided by thin lossy metal films of finite width: Bound modes of asymmetric structures," *Phys. Rev. B, Condens. Matter Mater. Phys.*, vol. 63, no. 12, p. 125 417, Mar. 2001.
[17] R. Zia, M. D. Selker, and M. L. Brongersma, "Leaky and bound modes of surface plasmon waveguides," *Phys. Rev. B, Condens. Matter Mater. Phys.*, vol. 71, no. 16, p. 165 431, Apr. 2005.
[18] R. F. Oulton, V. J. Sorger, D. A. Genov, D. F. P. Pile, and X. Zhang, "A hybrid plasmonic waveguide for subwavelength confinement and long-range propagation," *Nat. Photon.*, vol. 2, no. 8, pp. 496–500, Aug. 2008.
[19] H.-S. Chu, E.-P. Li, P. Bai, and R. Hegde, "Optical performance of single-mode hybrid dielectric-loaded plasmonic waveguide-based components," *Appl. Phys. Lett.*, vol. 96, no. 22, pp. 221103-1–221103-3, May 2010.
[20] Y. Binfeng, H. Guohua, J. Yang, and C. Yiping, "Characteristics analysis of a hybrid surface plasmonic waveguide with nanometric confinement and high optical intensity," *J. Opt. Soc. Amer. B*, vol. 26, no. 10, pp. 1924–1929, Oct. 2009.
[21] Y. Bian, Z. Zheng, X. Zhao, J. Zhu, and T. Zhou, "Symmetric hybrid surface plasmon polariton waveguides for 3D photonic integration," *Opt. Exp.*, vol. 17, no. 23, pp. 21 320–21 325, Nov. 2009.
[22] J. Chen, Z. Li, S. Yue, and Q. Gong, "Hybrid long-range surface plasmon-polariton modes with tight field confinement guided by asymmetrical waveguides," *Opt. Exp.*, vol. 17, no. 26, pp. 23 603–23 609, Dec. 2009.
[23] T. Holmgaard, J. Gosciniak, and S. I. Bozhevolnyi, "Long-range dielectric-loaded surface plasmon-polariton waveguides," *Opt. Exp.*, vol. 18, no. 22, pp. 23 009–23 015, Oct. 2010.
[24] Y. Kou, F. W. Ye, and X. F. Chen, "Low-loss hybrid plasmonic waveguide for compact and high-efficient photonic integration," *Opt. Exp.*, vol. 19, no. 12, pp. 11 746–11 752, Jun. 2011.
[25] P. Berini and R. Buckley, "On the convergence and accuracy of numerical mode computations of surface plasmon waveguides," *J. Comput. Theor. Nanosci.*, vol. 6, no. 9, pp. 2040–2053, 2009.
[26] Q. H. Liu, "A pseudospectral frequency-domain (PSFD) method for computational electromagnetics," *IEEE Antennas Wireless Propagat. Lett.*, vol. 1, no. 6, pp. 131–134, 2002.

[27] C.-C. Huang, "Numerical investigation of mode characteristics of nanoscale surface plasmon-polaritons using a pseudospectral scheme," *Opt. Exp.*, vol. 18, no. 23, pp. 23 711–23 726, 2010.
[28] M. Luo, Q. H. Liu, and Z. Li, "Spectral element method for band structures of two-dimensional anisotropic photonic crystals," *Phys. Rev. E, Stat. Nolin. Soft Matter Phys.*, vol. 79, no. 2, p. 026 705, Feb. 2009.
[29] M. Luo and Q. H. Liu, "Spectral element method for band structures of three-dimensional anisotropic photonic crystals," *Phys. Rev. E, Stat. Nolin. Soft Matter Phys.*, vol. 80, no. 5, p. 056702, Nov. 2009.
[30] G. C. Cohen, *Higher-Order Numerical Methods for Transient Wave Equations*. Berlin, Germany: Springer-Verlag, 2001.
[31] J.-H. Lee and Q. H. Liu, "An efficient 3-D spectral-element method for Schrödinger equation in nanodevice simulation," *IEEE Trans. Comput.-Aided Des. Integr. Circuits Syst.*, vol. 24, no. 12, pp. 1848–1858, Dec. 2005.
[32] J.-H. Lee, T. Xiao, and Q. H. Liu, "A 3-D spectral-element method using mixed-order curl conforming vector basis functions for electromagnetic fields," *IEEE Trans. Microw. Theory Tech.*, vol. 54, no. 1, pp. 437–444, Jan. 2006.
[33] D. Sarid and W. Challener, *Modern Introduction to Surface Plasmons: Theory, Mathematical Modeling, and Applications*. Cambridge, U.K.: Cambridge Univ. Press, 2010.
[34] T. Holmgaard and S. I. Bozhevolnyi, "Theoretical analysis of dielectric-loaded surface plasmon-polariton waveguides," *Phys. Rev. B, Condens. Matter Mater. Phys.*, vol. 75, no. 24, p. 245405, Jun. 2007.
[35] P. B. Johnson and R. W. Christy, "Optical constants of the noble metals," *Phys. Rev. B, Condens. Matter Mater. Phys.*, vol. 6, no. 12, pp. 4370–4379, Dec. 1972.
[36] R. F. Oulton, G. Bartal, D. F. P. Pile, and X. Zhang, "Confinement and propagation characteristics of subwavelength plasmonic modes," *New J. Phys.*, vol. 10, no. 10, p. 105018, Oct. 2008.